

## Article

# Interactions Between Trivalent Elements Enable Ultrastable LDH Cathode for High-Performance Zinc Battery

Junhua Zeng, Jinlei Gao, Wenyao Lu, Jiashuo Feng and Ting Deng \*

Key Laboratory of Automobile Materials of MOE, School of Materials Science and Engineering, and Jilin Provincial International Cooperation Key Laboratory of High-Efficiency Clean Energy Materials, Jilin University, Changchun 130012, China; zengjh1621@mails.jlu.edu.cn (J.Z.); gaojl1621@mails.jlu.edu.cn (J.G.); luwy1621@mails.jlu.edu.cn (W.L.); fengjs1621@mails.jlu.edu.cn (J.F.)

\* Correspondence: tdeng@jlu.edu.cn

**Abstract:** Layered double hydroxides (LDHs) are one class of two-dimensional materials, with tunable chemical composition and large interlayer spacing, that is a potential cathode material candidate for aqueous zinc-ion batteries (AZIBs). Nevertheless, the low conductivity and fragile structure of LDH have impeded their practical application in AZIBs. Herein, a ternary CoMnAl LDH is synthesized via the facile coprecipitation method as the cathode material for AZIB. The interaction between trivalent Al<sup>3+</sup> and Mn<sup>3+</sup> not only lowers the redox energy barrier but also enhances the electronic structure, as proved by EIS analysis and DFT simulation. As a result, the synthesized CoMnAl LDH displays a high specific capacity of 238.9 mAh g<sup>-1</sup> at 0.5 A g<sup>-1</sup>, an outstanding rate performance (138.8 mAh g<sup>-1</sup> at 5 A g<sup>-1</sup>), and a stable cyclability (92% capacity retention after 2000 cycles).

**Keywords:** layered double hydroxide; cathode material; electron interaction; aqueous zinc-ion battery

## 1. Introduction



Academic Editor: Marco Giorgetti

Received: 13 March 2025

Revised: 21 April 2025

Accepted: 22 April 2025

Published: 23 April 2025

**Citation:** Zeng, J.; Gao, J.; Lu, W.; Feng, J.; Deng, T. Interactions Between Trivalent Elements Enable Ultrastable LDH Cathode for High-Performance Zinc Battery. *Batteries* **2025**, *11*, 170. <https://doi.org/10.3390/batteries11050170>

**Copyright:** © 2025 by the authors. Licensee MDPI, Basel, Switzerland. This article is an open access article distributed under the terms and conditions of the Creative Commons Attribution (CC BY) license (<https://creativecommons.org/licenses/by/4.0/>).

As lithium ores become strategic resources, developing alternative high-performance electrochemical energy storage devices (EESDs) with high safety and low cost in the post-lithium age is of great significance for environmental and resource sustainability [1,2]. Aqueous zinc-ion batteries (AZIBs) have become a hot spot in EESD research due to the high specific capacity (820 mAh g<sup>-1</sup>) and high crustal content [3–5]. However, besides the dendrite issue, the application of AZIBs also suffers from the unsatisfying electrochemical performance of cathode materials, such as the low redox potential and unstable cycling life [6,7]. Therefore, investigations on cathode materials with high specific capacity, fast rate capability, and long cyclability are imperative for high-performance AZIBs.

Layered double hydroxides (LDHs) are a class of 2D layered materials, which can be represented by the general formula  $[M_{1-x}^{2+}M_x^{3+}(OH)_2]^{x+}[A^{n-}]_{x/n}\cdot yH_2O$  [8,9]. In this formula, M<sup>2+</sup> and M<sup>3+</sup> stand for divalent and trivalent metal cations occupying the octahedral holes in the brucite-like layer, while A<sup>n-</sup> stands for anions from the precursor located in the hydrated interlayer galleries (Figure 1A). It is explicit that the electrochemical performance of LDHs originates from the redox reaction of transition metal atoms during the charge/discharge process. The unique 2D morphology can expose massive atoms on the LDH's surface, which provide sufficient active sites for the electrochemical reaction [10,11]. And the tunable composition makes LDH quite adaptable in different EESDs as an electrode material. Co and Mn species have shown promising properties, indicating that CoMn LDH is one potential electrode material for use in AZIBs [12–15].

However, general issues of weak electronic conductivity and structural collapse still restrict CoMn LDH from real application. LDHs face large polarization and redox irreversibility due to their semi-conductor nature [16,17]. Moreover,  $Mn^{3+}$  species on 2D surfaces can accelerate the dissolution into electrolytes, compromising the structural stability. Very recently, ternary LDHs with a third transition metal element have exhibited outstanding electrochemical performance in supercapacitors, such as NiCoAl, NiCoMn, CoZnAl, and CoNiFe. These LDHs usually consist of two divalent transition metal elements and one trivalent transition metal element. Compared to divalent metal ions, trivalent metal ions show higher reactivity and act as a bridge to conduct electrons. Thus, doping a second trivalent metal element in CoMn LDH can effectively modify the electronic structure of ambient atoms and regulate the band-gap structure, thus not only increasing the carrier in the system and promoting electron conduction but also creating strong interaction with soluble species to stabilize the structure (Figure 1B).

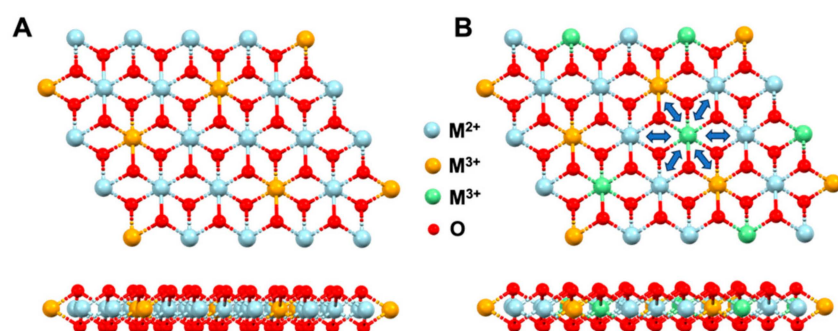


**Figure 1.** (A) An illustration of the LDH structure. (B) The structure of the LDH with one divalent and two trivalent transition metal elements.

Herein, a ternary CoMnAl LDH was synthesized via a coprecipitation method. As a AZIB cathode, CoMnAl LDH exhibited a high specific capacity of  $238.9 \text{ mAh g}^{-1}$  at  $0.5 \text{ A g}^{-1}$  and an outstanding rate performance ( $138.8 \text{ mAh g}^{-1}$  at  $5 \text{ A g}^{-1}$ ). X-ray photoemission spectroscopy (XPS) revealed that the valence of Mn species was partially increased by  $Al^{3+}$  introduction, while  $Co^{2+}$  remained, demonstrating that the interaction was between trivalent  $Mn^{3+}$  and  $Al^{3+}$ . Density functional theory (DFT) calculations confirmed the formation of a conductive CoMnAl-O network, which aligned with electrochemical impedance spectroscopy (EIS). In addition, both the overlap and the intensity of the density of state indicate that the structure of CoMnAl LDH was more stable. As a result, the performance of CoMn LDH decayed quickly within 500 cycles at  $0.5 \text{ A g}^{-1}$ . As a comparison, CoMnAl LDH showed a stable cycle life of 2000 cycles at the same current density with a capacity retention of 92%, which demonstrated the prospect of LDH for use as the cathode material of AZIBs.

## 2. Experimental Section

### 2.1. Synthesis of CoMn, CoAl, and CoMnAl LDHs

$Co(NO_3)_2$ ,  $Mn(NO_3)_2$ ,  $Al_2(SO_4)_3$ , and  $NH_3H_2O$  were all purchased from Aladdin Reagent Co., LTD (Shanghai, China). **CoMnAl:**  $Co(NO_3)_2$ ,  $MnSO_4$  and  $Al_2(SO_4)_3$  were dissolved in deionized water with a mole ratio of 6:2:2. Then,  $NH_3H_2O$  was dropwise added into the solution until no more sediment appeared. After a 30 min stirring period, the sediment was filtered and washed with deionized water, then put into a  $60^\circ\text{C}$  oven overnight. **CoMn** and **CoAl** were synthesized under the same procedure with a mole ratio of 6:4 (Co:Mn and Co:Al).

## 2.2. Physical Characterization

The X-ray diffraction tests of LDHs were conducted by a Bruker D8 powder diffractometer with a LynxEye XE-T detector. X-ray photoelectron spectroscopy, Raman spectroscopy and Fourier transform infrared spectroscopy were conducted by a Thermo ES-CALAB 250Xi tool, a Thermo DXR2 instrument, and a Perkin Elmer Spectrum One B device. The BET specific area was analyzed by N<sub>2</sub> adsorption measurements via an auto-JW-BK132F instrument from JWGB SCI. & TECH instruments. Scanning electron microscopy and transmission electron microscopy were performed by a Hitachi SU8000 scanning electron microscope and JEM ARM 1300S.

## 2.3. Electrochemical Evaluation

The electrochemical performances of LDHs were assessed in both a three-electrode system and a CR2032 coin cell. In the three-electrode system, a platinum plate and a saturated calomel electrode (SCE) served as the counter and reference electrodes. In the coin cell, Zn foil and a porous non-woven cloth served as the anode and separator. A total of 1 M KOH solution acted as the electrolyte in both the three-electrode system and coin cell. The electrolyte was prepared by dissolving 56 g of KOH pellets in 1000 mL of distilled water. The LDH cathode for AZIBs was fabricated as follows: LDH, acetylene black, and nafion (wt%: 8:1:1) were mixed in a small amount of ethanol for 12 h to make a homogeneous paste, which was coated onto carbon fiber paper as the current collector. Then, the electrode was put into a 60 °C oven overnight. The loading mass was ~2 mg/cm<sup>2</sup>. The charge/discharge profiles and cycling performance were determined by the Neware battery testing system, and cycling voltammetry and a Nyquist plot were carried out by a CHI660e potentiostat.

## 2.4. DFT Calculations

All theoretical calculations were performed by the use of density functional theory (DFT) with CASTEP code. The exchange/correlation energies were calculated using the generalized gradient approximation introduced by Perdew, Burke, and Ernzerhof. Ultrasoft pseudopotentials were conducted to describe the coupling between the ionic core and valence electrons, and the spin-polarized calculations were considered. The cutoff energy for the plane-wave basis set was set at 380.0 eV. For optimizing the cell, the convergence tolerance was  $5.0 \times 10^{-6}$  eV/atom to energy, 0.01 eV/Å to maximum force, 0.02 GPa to maximum stress, and  $5.0 \times 10^{-4}$  Å to maximum displacement. For geometric optimization and energy calculations, the separation of *k*-point sampling was adopted with 0.07/Å and 0.06/Å, respectively. A convergence accuracy of  $5.0 \times 10^{-7}$  eV/atom was set for the self-consistent field calculation. In our work, the mixtures of different elements were created. Mixture atoms can simulate disorder in a structure, such as in the case where one atomic site is randomly occupied by two or more different types of atoms.

## 3. Results and Discussion

CoMnAl LDH was synthesized by a facile coprecipitation method, as shown in Figure 2A, in which Co, Mn, and Al hydroxides shared edges and octahedral sheets bounded together. The crystalline structure of CoMnAl LDH was characterized by X-ray diffraction (XRD). Figure 2B displays the XRD patterns of CoMnAl LDH and CoMn counterpart, both of which show the typical (006) peak located around 20.6° [18]. The intensity of the (006) peak was enhanced after Al<sup>3+</sup> introduction, while (100) and (110) peaks were reduced. This was probably due to the layer charge density being affected by the charge and size of the metal ions in LDH. The calculated d<sub>006</sub> was 0.435 nm, which decreased to 0.433 nm after Al<sup>3+</sup> introduction (Table S1). To compensate these positive charges, anions from precursor solutions usually

absorb and occupy the interlayer spacing between LDH layers. Figure 2C depicts the Fourier transform infrared spectroscopy (FTIR) spectra of CoMnAl and CoMn LDHs. In both spectra, one can see that peaks located around  $1500\text{ cm}^{-1}$  are due to the N-O stretching mode and the peak centered at  $1120\text{ cm}^{-1}$  is due to the S-O stretching vibration, indicating  $\text{NO}_3^-$  and  $\text{SO}_4^{2-}$ , intercalated into the layer structure [19,20]. The broad band at  $3470\text{ cm}^{-1}$  can be assigned to the O-H vibration from the OH group and interlayer water. The peaks at around  $600\text{ cm}^{-1}$  are the characteristic of Co/Mn/Al-O and Co/Mn/Al-OH bending vibrations, respectively.

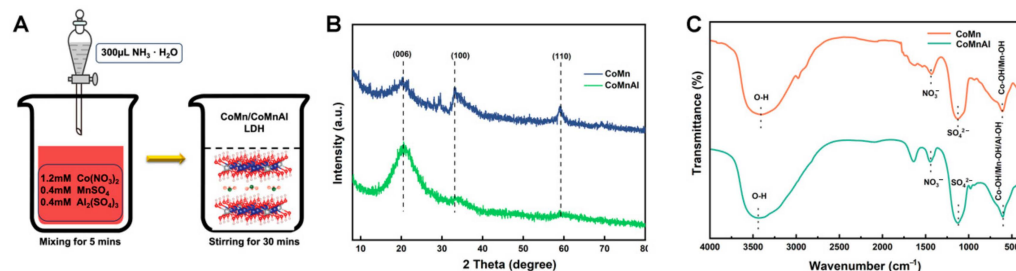


**Figure 2.** (A) An illustration of LDH synthesis. (B,C) The XRD and FTIR spectra of CoMn and CoMnAl.

Scanning electron spectroscopy (SEM) and transmission microscopy (TEM) were conducted to analyze the morphologies of CoMnAl and CoMn LDHs. Figure 3A shows that CoMn LDH displayed a plicated and porous particle morphology in nano-scale. Figure 3B confirms the character-layered structure of LDH. The lattice fringe was calculated to be  $2.71\text{ \AA}$ , corresponding to  $d_{100}$ -spacing. In the LDH layer, transparent regions are observed, indicating that pores with an average diameter of 20–30 nm (P stands for pore structure) exist in these LDH layers. The specific surface area of CoMn LDH was examined by nitrogen adsorption (Figure 3C). The Brunauer–Emmett–Teller (BET) surface area of the CoMn LDH was calculated to be  $47.260\text{ m}^2\text{g}^{-1}$ . Figure 3D exhibits the SEM image of CoMnAl LDH, in which more pores were detected. The layered structure of the CoMnAl LDH was also confirmed by HRTEM, but the pore diameter was increased, with an average size of 10 nm (Figure 3E). Accordingly, the BET surface area increased to  $106.530\text{ m}^2\text{g}^{-1}$  (Figure 3F). The increased BET surface and porous structure were attributed to  $\text{Al}^{3+}$ , with a smaller size and high charge strongly affecting the charge density of the LDH layers.

To further probe the influence of  $\text{Al}^{3+}$  introduction to the LDH surface state, X-ray photoemission spectroscopy (XPS) measurement was carried out. Figure 4A shows the Co 2p XPS spectrum in CoMnAl LDH. The binding energies of 797.1 eV and 781.5 eV for  $2\text{p}_{1/2}$  and  $2\text{p}_{3/2}$  were observed as photoemission maxima, with two satellite structures. In the fitted curve, the main peak of Co 2p<sub>3/2</sub> centering at 780.5 eV is typical evidence of  $\text{Co}^{2+}$  species [21]. The valence of the Co element was also demonstrated to be +2 in CoMn (Figure 4B) and CoAl LDHs (Figure 4C), suggesting that Mn and Al had no effects on the electronic structure of Co element. The Mn 2p XPS spectra of CoMn and CoMnAl LDHs are displayed in Figure 4D,E. In the fitted curve of CoMn LDH, the main peak of Mn 2p<sub>2/3</sub> is located at 642.3 eV, implying that the valence state of the Mn species was +3 [22]. But the increased content of  $\text{Mn}^{4+}$  species was observed in CoMnAl LDH, while the valence of Co element remained. In CoAl LDH, the valence state of Al was evidenced to be +3, since the main peak was located at 75 eV (Figure 4F). Nevertheless, the main peak of Al 2p negatively shifted by 0.47 eV, which indicates the decrease in Al valence in CoMnAl. It seems that partial  $\text{Al}^{3+}$  substitution with high charge density caused stronger electronic interaction with ambient trivalent Mn than bivalent Co species.

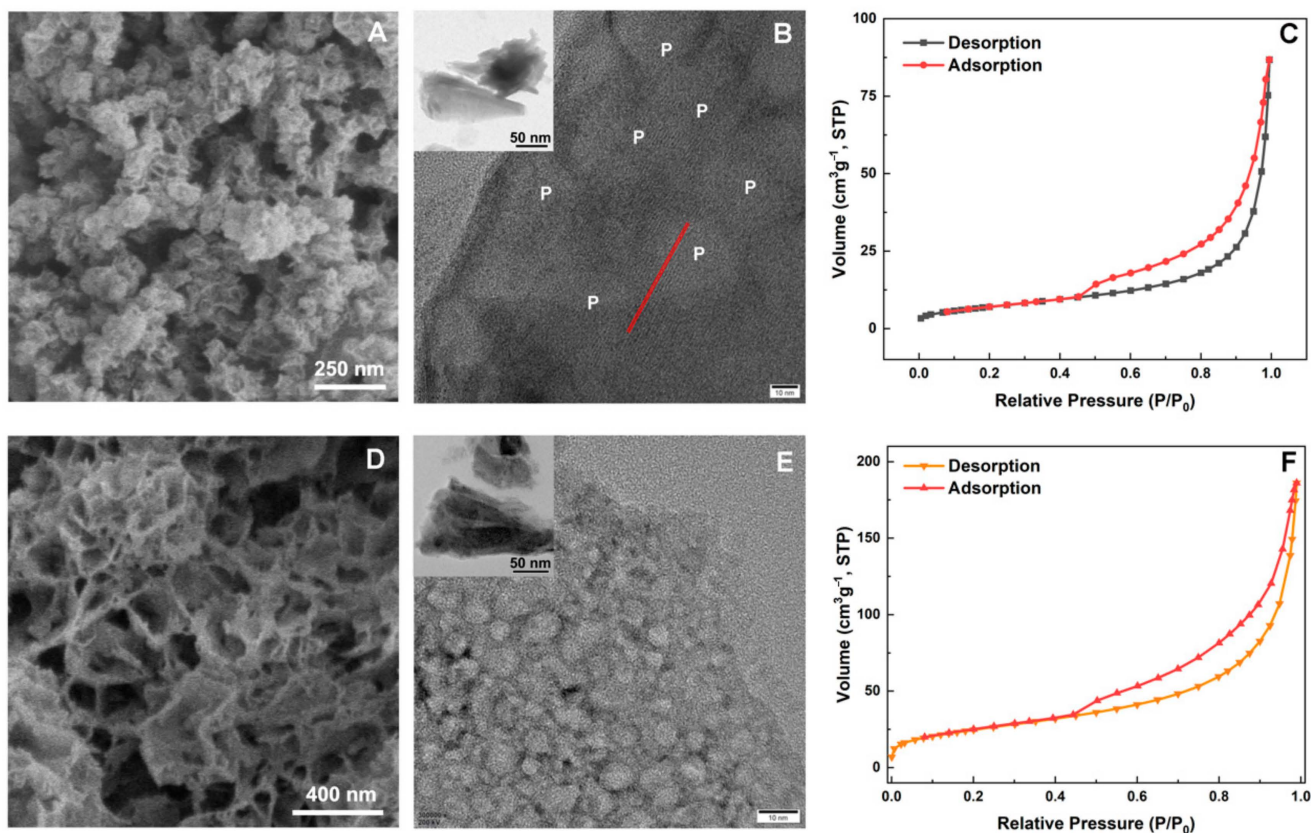


**Figure 3.** (A–C) SEM, TEM, and HRTEM images and N<sub>2</sub> isotherm of CoMn LDH. (D–F) SEM, TEM, and HRTEM images and N<sub>2</sub> isotherm of CoMnAl LDH.

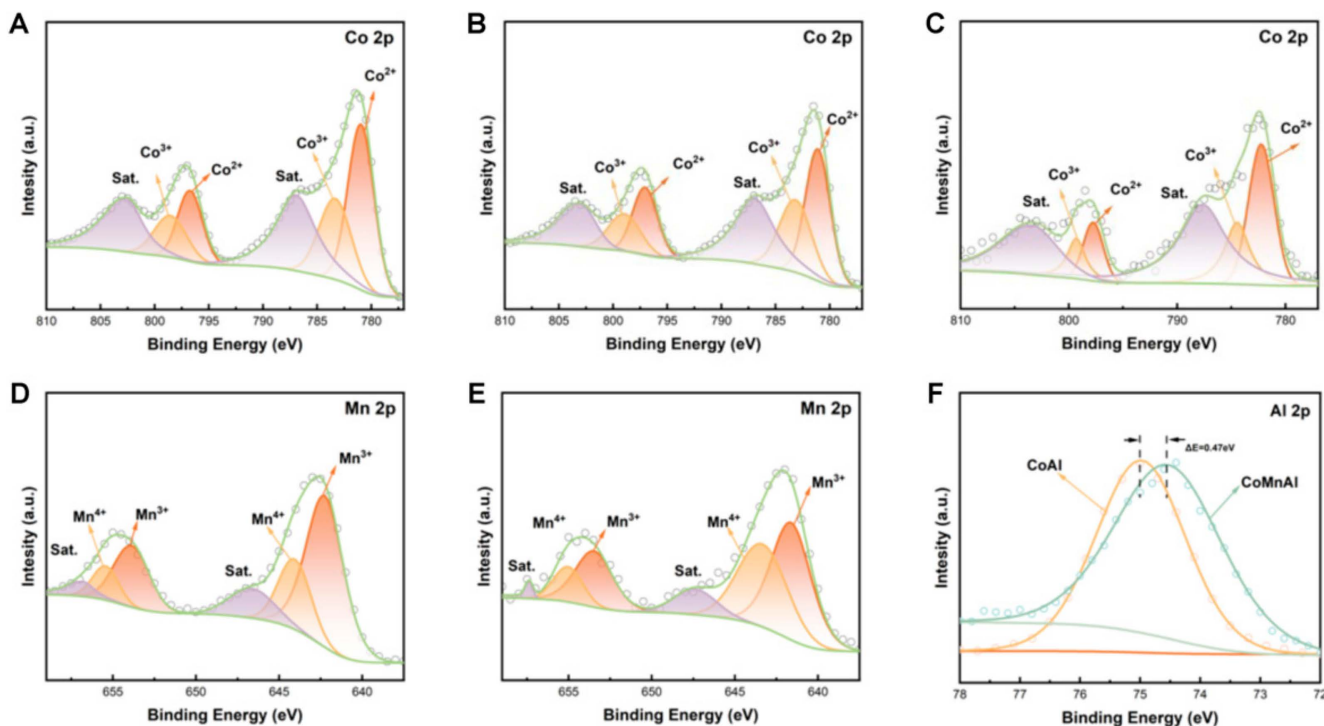


**Figure 4.** (A–C) XPS spectra of Co 2p in CoMnAl, CoMn, and CoAl LDHs. (D,E) XPS spectra of Mn 2p in CoMn and CoMnAl. (F) Comparison of Al 2p in CoAl and CoMnAl.

Further, we employed DFT to calculate their electronic structures, and the results are shown in Figure 5. It was found that their bands consist of three parts in general, which are

marked by dashed rectangles. The bands in the top part are nearly empty, and the bands in the bottom part are full of electrons. In contrast, the Fermi level goes through the middle part containing the bands composed of mainly d orbitals and a small number of p orbitals. Noticeably, the bands in the top part are the most dispersed, and the bands in the middle part are the most localized. Alpha and beta represent the bands of electrons with upward and downward spin directions, respectively. For  $\text{Co(OH)}_2$ , the top part overlaps slightly with the middle part, implying that they are partially hybrid. The gap is about 2.05 eV between the middle and bottom parts. In addition, the spin polarization clearly appears near the Fermi level due to the presence of the Co atom, which mainly occurs in the middle part. When 40% of the Mn element is introduced into  $\text{Co(OH)}_2$ , the bimetallic component  $\text{CoMn LDH}$  is formed. It was observed that the bands near the Fermi level are degenerate. Such degenerate orbitals cause the energy region in the middle part to become narrow compared with  $\text{Co(OH)}_2$ . Accordingly, the density of states (DOS) near the Fermi level also obviously increases. The gap is widened to 3.28 eV between the middle and bottom parts. When Al is further introduced, the trimetallic component of  $\text{CoMnAl LDH}$  can be also synthesized. It was found that the bands in the top and bottom parts shift upwards due to electron deficiency. The elevation of the bands in the top part leads to overlap decrease between the top and middle parts, which means less hybridization. Sequentially, the bands in the middle part further narrow and the DOS appears sharply. The gap is narrowed to 1.68 eV between the middle and bottom parts. Due to fewer electrons being present, the spin polarization reappears near the Fermi level. When one component of the bimetallic component of hydroxide is Al ( $\text{CoAl LDH}$ ), the bands in the top and bottom parts further shift upwards. A gap is formed between the top and middle parts. In contrast, the bands in the bottom part enter into the middle part, resulting in significant orbital hybridization and some spin polarization. The dispersed behavior widens the bands in the middle part, and the corresponding DOS is less sharp. The strength of the M-O bond (M: metals atoms) can be evaluated by the bands in the bottom part, and activity can be assessed by the bands in the middle part. They are analyzed from their corresponding DOSs. It was observed that the peaks in the bottom part are mainly hybridized by the states of metals and oxygen for  $\text{CoMn}$ ,  $\text{CoAl}$ , and  $\text{CoMnAl LDHs}$ . In particular, for the top peak, its overlap and intensity suggest that the crystalline structure of  $\text{CoMnAl LDH}$  is the most stable among them. For the  $\text{CoMnAl LDH}$ , a sharp peak at the Fermi level means that metals have the very localized electrons. Such nonbonding electrons are conducive to the activation of metals. In addition, it was observed that, for  $\text{CoMn LDH}$ , the electrons of  $\text{CoAl LDH}$  at the Fermi level are more localized than those of  $\text{Co(OH)}_2$ , and the bands of  $\text{CoAl LDH}$  near the Fermi level are more dispersed than those of  $\text{Co(OH)}_2$ , indicating that  $\text{CoAl LDH}$  is more conductive.

The electrochemical performances of  $\text{CoMn}$  and  $\text{CoMnAl LDHs}$  were examined in a coin cell (Figure 6A), in which LDHs, Zn foil, and 1 M KOH solution were utilized as the cathode, anode, and electrolyte, respectively. The open-circuit voltages of Zn-CoMn and Zn-CoMnAl cells were 1.15 and 1.21 V. Accordingly, the Zn-CoMnAl cell displayed a better electrochemical performance. Figure 6B exhibits the charge/discharge profiles of the Zn-CoMnAl cell at different current densities. Two discharge plateaus indicate a stepwise reaction mechanism, corresponding to Co and Mn redox. At a current density of  $0.5 \text{ A g}^{-1}$ , the Zn-CoMnAl cell deliver a high specific capacity of  $238.9 \text{ mAh g}^{-1}$ . On the other hand, the Zn-CoMn cell displays an inferior electrochemical performance (Figure 6C). Two discharge plateaus remain, but the discharge time is much shorter. The Zn-CoMn cell only showed a capacity of  $159 \text{ mAh g}^{-1}$  at  $0.5 \text{ A g}^{-1}$ , and the capacity was 81.2, 68.6, and  $51.2 \text{ mAh g}^{-1}$  as the current density increased to 1, 2, and  $5 \text{ A g}^{-1}$ , respectively. In contrast, an excellent rate capability was obtained by the Zn-CoMnAl cell at the same current density (194.75, 179.05, and  $138.75 \text{ mAh g}^{-1}$  at 1, 2, and  $5 \text{ A g}^{-1}$ , respectively; Figure 6D).

The cyclic voltammetry (CV) curves of Zn-CoMnAl and Zn-CoMn cells are depicted in Figure 6E. The CV test starts from 0.6 V to a high voltage, and the arrows represent the directions of oxidation and reduction scans. The CV curve of Zn-CoMnAl shows a higher peak current and larger enclosed area than that of Zn-CoMn, implying higher activity after Al<sup>3+</sup> introduction. To gain more insight into the effect of Al<sup>3+</sup> introduction in CoMnAl LDH, electrochemical impedance spectroscopy (EIS) was conducted in a three-electrode system. Figure 6F shows the Nyquist plots of the CoMnAl and CoMn LDHs, obtained at ambient temperature. R<sub>ct</sub> in electrical equivalent circuit (Figure 6F inset) stands for charge-transfer resistance. The calculated R<sub>ct</sub> of CoMnAl LDH is 2.5 Ω, while the R<sub>ct</sub> of CoMn is 3.6 Ω, indicative of a low resistance of electron transfer from the interface between the LDH and the electrolyte and a higher energy storage efficiency resulting from Al<sup>3+</sup> introduction. Furthermore, the activation energy was calculated as 1.4 V, at which potential the charge process initiated. The activation energy was examined based on a series of EIS tests at different temperatures, representing the energy barrier of Co and Mn redox reactions (Figure 6G,H). The activation energy of the Zn-CoMnAl cell is 16.28 kJ mol<sup>-1</sup> was lower than that of the Zn-CoMn cell (28.56 kJ mol<sup>-1</sup>) and could be attributed to a highly conductive CoMnAl-O network. The lower energy barrier of the CoMnAl LDH could also lead to a high conversion efficiency and structural stability. In accordance with DFT simulation, the capacity of the Zn-CoMn cell dropped quickly within 500 cycles at 0.5 A g<sup>-1</sup> (76% retention), while the Zn-CoMnAl cell showed a stable cycle life of 2000 cycles at the same current density with a capacity retention of 92%.

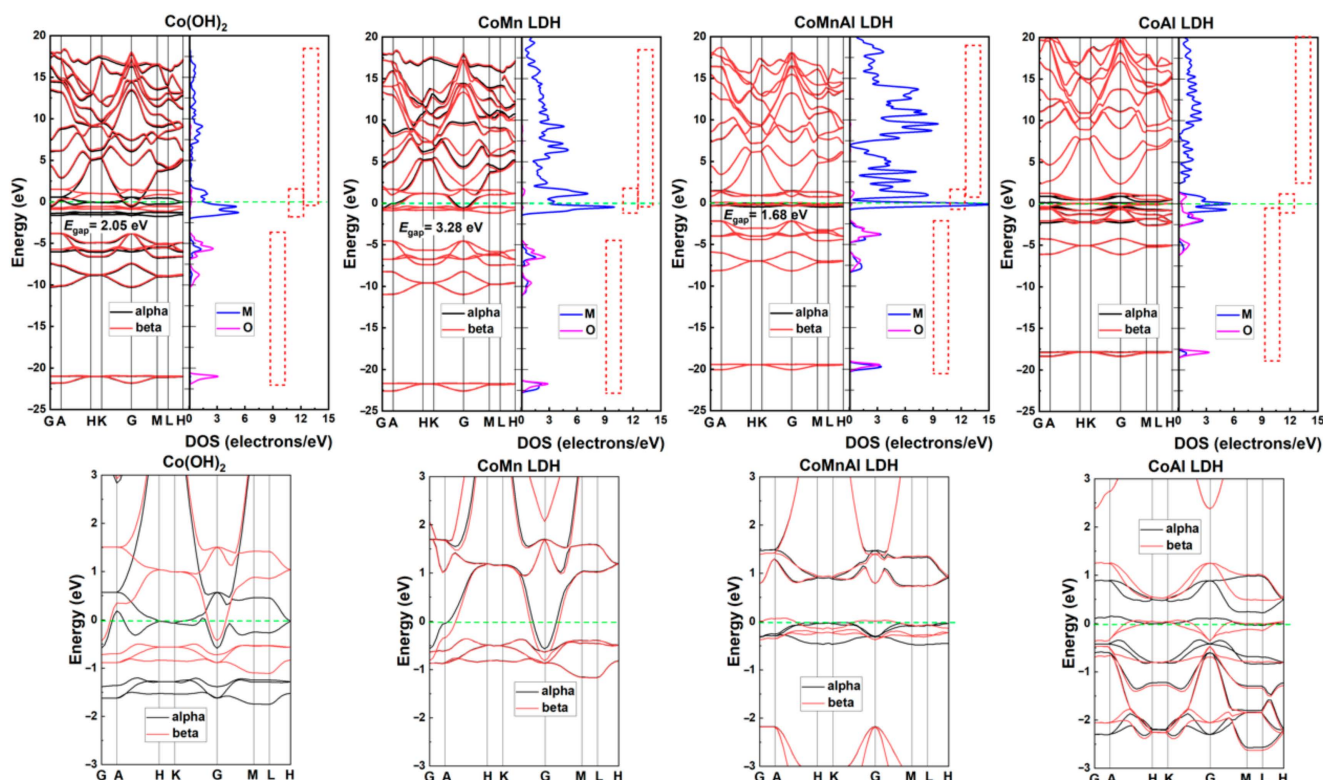


**Figure 5.** The energy bands (left) and density of states (right) for different structures. M and O denote metal and oxygen atoms, respectively. The spectra in the bottom panel show the magnified images of the band dispersion near the Fermi level. The Fermi level is set to 0 eV. Inset: the dashed rectangles schematically indicate different band parts.

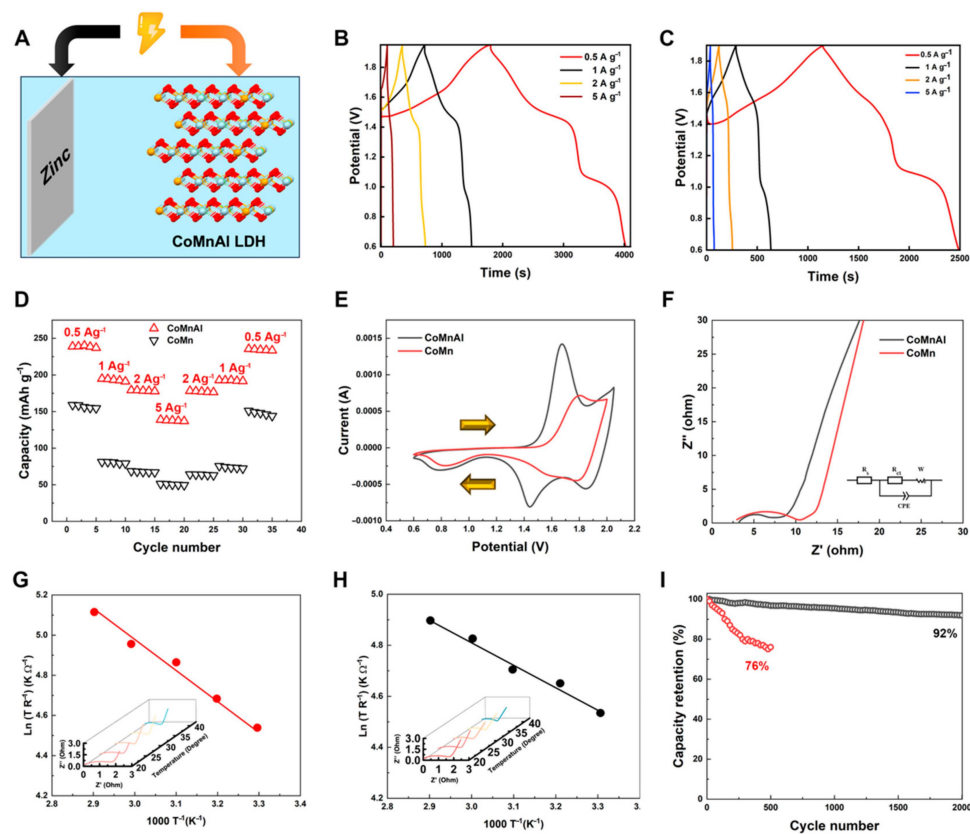


**Figure 6.** (A) The AZIB with CoMnAl LDH cathode and zinc anode. (B,C) The charge/discharge profiles of Zn-CoMnAl and Zn-CoMn AZIB cells at different current densities. (D) The rate capability of Zn-CoMnAl and Zn-CoMn AZIB cells. (E) A CV comparison of Zn-CoMnAl and Zn-CoMn AZIB cells at a scan rate of  $4 \text{ mVs}^{-1}$ . (F) The Nyquist plots and the equivalent electrical circuit. (G,H) The EIS curves of Zn-CoMn and Zn-CoMnAl AZIB cells at different temperatures. (I) The cyclability of Zn-CoMn and Zn-CoMnAl AZIB cells.

#### 4. Conclusions

In summary, CoMnAl LDH is synthesized via a facile coprecipitation method, and it has proved to be promising as a cathode material for AZIB. The interaction between trivalent Mn and Al element not only lowers the intrinsic resistance and redox energy barrier but also strengthens the electronic structure and the electrochemical stability of LDH, as demonstrated by the DFT simulation and cycling performance. All these results demonstrate the prospects of LDH as a cathode material for AZIBs.

**Supplementary Materials:** The following supporting information can be downloaded at: <https://www.mdpi.com/article/10.3390/batteries11050170/s1>, Table S1: Interlayer spacings of CoMn and CoMnAl LDHs.

**Author Contributions:** Conceptualization, T.D.; methodology, T.D.; software, J.Z., J.G., W.L. and J.F.; validation, J.Z., J.G., W.L. and J.F.; formal analysis, J.Z. and J.G.; investigation, J.Z., J.G., W.L. and J.F.; resources, T.D.; data curation, T.D.; writing—original draft preparation, J.Z. and J.G.; writing—review and editing, T.D.; visualization, T.D.; supervision, T.D.; project administration, T.D. All authors have read and agreed to the published version of the manuscript.

**Funding:** This work was supported by the International Collaboration Program of the Jilin Provincial Department of Science and Technology (No. 20230402051GH), the 2024 Innovation-High-tech Industry Program of Jilin Province Development and Reform Commission (No. 2024C018-8), the Fundamental Research Funds for the Central Universities, JLNU, and the “Double-First Class” Discipline for Materials Science & Engineering.

**Data Availability Statement:** The raw data supporting the conclusions of this article will be made available by the authors on request.

**Conflicts of Interest:** The authors declare no conflicts of interest.

## References

1. Ma, W.; Wang, S.; Wu, X.; Liu, W.; Yang, F.; Liu, S.; Jun, S.C.; Dai, L.; He, Z.; Zhang, Q. Tailoring desolvation strategies for aqueous zinc-ion batteries. *Energy Environ. Sci.* **2024**, *17*, 4819–4846. [[CrossRef](#)]
2. Zheng, X.; Han, C.; Lee, C.-S.; Yao, W.; Zhi, C.; Tang, Y. Materials challenges for aluminum ion based aqueous energy storage devices: Progress and prospects. *Prog. Mater. Sci.* **2024**, *143*, 101253. [[CrossRef](#)]
3. Li, C.; Hu, L.; Ren, X.; Lin, L.; Zhan, C.; Weng, Q.; Sun, X.; Yu, X. Asymmetric Charge Distribution of Active Centers in Small Molecule Quinone Cathode Boosts High-Energy and High-Rate Aqueous Zinc-Organic Batteries. *Adv. Funct. Mater.* **2024**, *34*, 2313241. [[CrossRef](#)]
4. Guo, X.; Zhang, S.; Hong, H.; Wang, S.; Zhu, J.; Zhi, C. Interface regulation and electrolyte design strategies for zinc anodes in high-performance zinc metal batteries. *iScience* **2025**, *28*, 111751. [[CrossRef](#)]
5. Peng, Z.; Shen, X.; Li, B.; Cheng, J.; He, Z.; Sun, Z.; Li, B.; Zhang, Z.; Zhuang, Z.; Wu, X.; et al. Comprehensive crystallographic engineering for high-efficiency and durable zinc metal anodes. *Prog. Mater. Sci.* **2025**, *152*, 101453. [[CrossRef](#)]
6. Cao, J.; Wu, H.; Zhang, D.; Luo, D.; Zhang, L.; Yang, X.; Qin, J.; He, G. In-Situ Ultrafast Construction of Zinc Tungstate Interface Layer for Highly Reversible Zinc Anodes. *Angew. Chem. Int. Ed.* **2024**, *63*, e202319661. [[CrossRef](#)]
7. Cao, J.; Sun, M.; Zhang, D.; Zhang, Y.; Yang, C.; Luo, D.; Yang, X.; Zhang, X.; Qin, J.; Huang, B.; et al. Tuning Vertical Electrodeposition for Dendrites-Free Zinc-Ion Batteries. *ACS Nano* **2024**, *18*, 16610–16621. [[CrossRef](#)]
8. Chen, F.; Li, J.; Shao, Y.; Zhu, Z.; Shen, T.; Chen, K.; Chen, Y.; Chen, Y. ZIF-67 wraps Ni-Mn LDHs nanosheets to enhance the capacitive contribution of supercapacitors. *Chem. Eng. J.* **2025**, *507*, 160454. [[CrossRef](#)]
9. Zhang, S.; Zhao, Y.; Gao, S.; Liu, C.; Chen, X. Design and synthesis of nickel-cobalt-aluminum hydroxide battery electrode materials for high-performance hybrid supercapacitors. *J. Power Sources* **2025**, *632*, 236370. [[CrossRef](#)]
10. Wang, C.; Wang, D.; Lv, D.; Peng, H.; Song, X.; Yang, J.; Qian, Y. Interface Engineering by Hydrophilic and Zincophilic Aluminum Hydroxide Fluoride for Anode-Free Zinc Metal Batteries at Low Temperature. *Adv. Energy Mater.* **2023**, *13*, 2204388. [[CrossRef](#)]
11. Zhao, Y.; Zhang, P.; Liang, J.; Xia, X.; Ren, L.; Song, L.; Liu, W.; Sun, X. Unlocking Layered Double Hydroxide as a High-Performance Cathode Material for Aqueous Zinc-Ion Batteries. *Adv. Mater.* **2022**, *34*, e2204320. [[CrossRef](#)] [[PubMed](#)]
12. Li, Q.; Wang, C.; Zhu, Y.; Du, W.; Liu, W.; Yao, M.; Wang, Y.; Qian, Y.; Feng, S. Unlocking the critical role of Mg doping in  $\alpha$ -MnO<sub>2</sub> cathode for aqueous zinc ion batteries. *Chem. Eng. J.* **2024**, *485*, 150077. [[CrossRef](#)]
13. Zhao, X.; Zhang, F.; Li, H.; Dong, H.; Yan, C.; Meng, C.; Sang, Y.; Liu, H.; Guo, Y.-G.; Wang, S. Dynamic heterostructure design of MnO<sub>2</sub> for high-performance aqueous zinc-ion batteries. *Energy Environ. Sci.* **2024**, *17*, 3629–3640. [[CrossRef](#)]
14. Liang, X.; Liu, X.; Wang, P.; Guo, Z.; Chen, X.; Yao, J.; Li, J.; Gan, Y.; Lv, L.; Tao, L.; et al. Ion-exchange induced Ni doping of  $\alpha$ -MnO<sub>2</sub> cathode with structural modification for aqueous zinc ion batteries. *J. Power Sources* **2025**, *635*, 236518. [[CrossRef](#)]
15. Fu, H.; Wang, X.; Ye, L.; Wu, Z.; Yang, J.; Shi, M.; Ang, E.H. Optimizing Fe in Mn-based Prussian blue analogs with dual redox-active sites to enhance operating voltage and durability in Zn-ion batteries. *Chem. Eng. J.* **2025**, *506*, 160308. [[CrossRef](#)]
16. Zhang, Y.; Hu, S.; Li, C.-e.; Yan, X.-h.; Zhang, Y.-y.; Yin, R.-b.; Wei, Y.-f.; Gao, K.-z.; Gao, H.-l. Advanced strategies for enhancing electrochemical performance of NiAl LDH electrodes in supercapacitors. *Coord. Chem. Rev.* **2025**, *531*, 216497. [[CrossRef](#)]
17. Bai, S.; Liu, G.; Shen, T.; Wu, Z.; Chen, W.; Song, Y.-F. Controllable synthesis of layered double hydroxides: From macroscopic morphology to microscopic coordination at the atomic level. *Coord. Chem. Rev.* **2025**, *529*, 216437. [[CrossRef](#)]
18. Bujdosó, T.; Patzkó, Á.; Galbács, Z.; Dékány, I. Structural characterization of arsenate ion exchanged MgAl-layered double hydroxide. *Appl. Clay Sci.* **2009**, *44*, 75–82. [[CrossRef](#)]
19. Wang, H.; Lin, T.; Song, Z.; Huang, M.; Chai, R.; An, S.; Song, Y.-F. Simultaneous mineralization of Cd(II), Pb(II) and As(V) using MgAl-NO<sub>3</sub>: Performance and mechanism. *Sep. Purif. Technol.* **2025**, *362*, 131853. [[CrossRef](#)]
20. Zhang, F.; Liu, L.; Zhang, C.; Shang, D.; Wu, L. Preparation of ZnAl layered double hydroxides supported by silica for the treatment of Cr(VI) and Cu(II) in aqueous solution. *Sci. Rep.* **2025**, *15*, 2522. [[CrossRef](#)]
21. Wang, C.; Han, L.; Yang, S.; Liu, Z.; Liu, M.; Li, B. Nanosheet-structured ZnCo-LDH microsphere as active material for rechargeable zinc batteries. *J. Colloid Interface Sci.* **2024**, *659*, 119–126. [[CrossRef](#)] [[PubMed](#)]
22. Moradi, M.; Afkhami, A.; Madrakian, T.; Moazami, H.R. Electrosynthesis of Co Mn layered-double-hydroxide as a precursor for Co-Mn-MOFs and subsequent electrochemical sulfurization for supercapacitor application. *J. Energy Storage* **2023**, *71*, 108177. [[CrossRef](#)]

**Disclaimer/Publisher’s Note:** The statements, opinions and data contained in all publications are solely those of the individual author(s) and contributor(s) and not of MDPI and/or the editor(s). MDPI and/or the editor(s) disclaim responsibility for any injury to people or property resulting from any ideas, methods, instructions or products referred to in the content.